Dong, Hua; Xi, Jun; Zuo, Lijian; Li, Jingrui; Yang, Yingguo; Wang, Dongdong; Yu, Yue; Ma, Lin; Ran, Chenxin; Gao, Weiyin; Jiao, Bo; Xu, Jie; Lei, Ting; Wei, Feijie; Yuan, Fang; Zhang, Lin; Shi, Yifei; Hou, Xun; Wu, Zhaoxin

Conjugated Molecules “Bridge”

Published in:
Advanced Functional Materials

DOI:
10.1002/adfm.201808119

Published: 25/04/2019

Document Version
Peer reviewed version

Please cite the original version:
Dong, H., Xi, J., Zuo, L., Li, J., Yang, Y., Wang, D., Yu, Y., Ma, L., Ran, C., Gao, W., Jiao, B., Xu, J., Lei, T., Wei, F., Yuan, F., Zhang, L., Shi, Y., Hou, X., & Wu, Z. (2019). Conjugated Molecules “Bridge”: Functional Ligand toward Highly Efficient and Long-Term Stable Perovskite Solar Cell. *Advanced Functional Materials*, *29*(17), 1-11. [1808119]. https://doi.org/10.1002/adfm.201808119

DOI: 10.1002/adfm.201808119
Article type: Full Paper

Conjugated Molecules "Bridge": Functional Ligand toward Highly Efficient and Long-Term Stable Perovskite Solar Cell

Hua Dong [1,3#], *Jun Xi* [2#], *Lijian Zuo* [4], *Jingrui Li* [5], *Yingguo Yang* [6], *Dongdong Wang* [7], *Yue Yu* [7,8], *Lin Ma* [8], *Chenxin Ran* [1,3], *Weiyin Gao* [1], *Bo Jiao* [1], *Jie Xu* [1], *Ting Lei* [1], *Feijie Wei* [1], *Fang Yuan* [1], *Lin Zhang* [1], *Yifei Shi* [1], *Xun Hou* [1], *and Zhaoxin Wu* [1,3]*

[1] Key Laboratory for Physical Electronics and Devices of the Ministry of Education & Shaanxi Key Lab of Information Photonic Technique School of Electronic and Information Engineering, Xi'an Jiaotong University, No. 28, Xianning West Road, Xi'an 710049, China

[2] Global Frontier Center for Multiscale Energy Systems, Seoul National University, Seoul 08826, Korea

[3] Collaborative Innovation Center of Extreme Optics, Shanxi University, Taiyuan 030006, China

[4] Department of Materials Science and Engineering, University of Washington, Seattle, WA 98195, USA

[5] Department of Applied Physics, Aalto University, FI-00076, Aalto Finland

[6] Shanghai Synchrotron Radiation Facility, Shanghai Institute of Applied Physics, Chinese Academy of Sciences, Shanghai 201204, China

[7] Department of Chemistry, School of Science, Xi'an Jiaotong University, Xi'an 710049, China

[8] School of Physics and Optoelectronic Engineering, Xidian University, Xi'an 710071, China

***Corresponding author. E-mail: zhaoxinwu@mail.xjtu.edu.cn**
[#] These two authors contributed to this work equally.

Abstract

Interfacial ligand passivation engineering has recently been recognized as a promising avenue, contributing simultaneously to the optoelectronic characteristics and moisture/operation tolerance of perovskite solar cells. To further achieve a win-win situation of both performance and stability, an innovative conjugated aniline modifier (3-phenyl-2-propen-1-amine; PPEA) is explored to moderately tailor organolead halide perovskites films. Here, the conjugated PPEA presents both "quasi-coplanar" rigid geometrical configuration and distinct electron delocalization characteristics. After a moderate treatment, a stronger dipole capping layer can be formed at the perovskite/transporting interface to achieve favorable banding alignment, thus enlarging the built-in potential and promoting charge extraction. Meanwhile, a conjugated cation coordinated to the surface of the perovskite grains/units can form preferably ordered overlapping, not only passivating the surface defects but also providing a fast path for charge exchange. Benefiting from this, a ≈21% efficiency of the PPEA-modified solar cell can be obtained, accompanied by long-term stability (maintaining 90.2% of initial power conversion efficiency after 1000 h testing, 25°C, and 40 ± 10 humidity). This innovative conjugated molecule "bridge" can also perform on a larger scale, with a performance of 18.43% at an area of 1.96 cm^2.

Keywords: conjugation, delocalization, interfacial dipole, perovskite, solar cells

INTRODUCTION

Inorganic–organic hybrid perovskite materials have drawn extensive attention in the photovoltaic community due to the advantages such as high absorption coefficient, excellent carrier mobility, and tunable bandgap [1–3]. Huge successes of perovskite solar cells (PSCs) have been achieved with the outstanding certified power conversion efficiency (PCE) of 23.7% in just several years [4–6]. However, further overcoming the performance limitation and achieving the long-term stability of the PSCs simultaneously are still critical issues in commercial applications [7–9]. Reports show that owing to the low formation energies, the formation of the perovskite polycrystalline film is always accompanied with the vacancy, substitutions, and interstitial defects inevitably [10,11]. These defects, whether on interiors or surface of the perovskite film, could play the role of the charge recombination centers, leading to trap-assisted non-radiative recombination losses [12,13]. Moreover, materials decomposition and ion migration could become more pronounced at the perovskite surface and grain boundaries (GBs), severely undermining the moisture and operating stability of the devices [14,15]. Recently, various technologies were developed to enhance the performance and stability of the perovskite films [16–19]. Among them, interface engineering strategy by means of ligands with coordination group is a facial and well-controlled way to endow the perovskite films excellent optoelectronic characteristics and moisture tolerance, and functional aniline/alkyl-amine ligands are widely applied as the representative objects [20–23]. Early study shows that alkyl-amines could successfully passivate perovskite surface and GBs via interaction with the under-coordinated halide anion of perovskite units through a noncovalent hydrogen bonding interaction, which enhances both the crystallization and the ambient stability of perovskite film, thus serving for the device performance [13]. Recently, anilines were chosen as the passivation molecules due to the hydrophobic benzene ring, and typical post-treatment process could impose an in situ formed 2D perovskite layer onto the pristine 3D perovskite substratum [24–28]. Owing to the hydrophobic feature of the large organic cations in 2D perovskite, emerging capping layer exhibited significantly enhanced long-term stability with respect to the 3D segments by effectively blocking the moisture invasion pathway from the external atmosphere. Meanwhile, wide bandgap property of the 2D material could modify the interface energy level, in favor of the charge extractions and recombination suppression [29,30].

Though there is efficient passivation of the long-chain organic components, charge transporting in the modified perovskite film is still discouraged. Subjecting to the typical long-chain/large-size construction, conventional ligands could not provide the efficient electrical channels across the perovskite framework, inducing a trade-off between defect elimination and charge transporting promotion [7,8,31]. This adverse impact may limit the maximized promotion of the device performance. Moreover, large-size aniline/alkyl-amine molecules could anchor to the surface and grains/units of the perovskite films with certain orientation on account of the stronger steric hindrance and rigidity features [32–34]. However, the structure order characteristic of the molecular effect on the interfacial polarity of the perovskite/transporting layers is rarely discussed. Hence, the design of ideal interfacial modifiers and deep understanding of the fundamentals of the interfacial passivation engineering are highly imperative to ultimately boost the PSC efficiency.

Based on this, a designed conjugated aniline ligand, namely, 3-phenyl-2-propen-1-amine (PPEA), was first explored to achieve the effective interface/interior modification of the perovskite photoactive layer via a post-treatment method. According to the systematically experimental and theoretical study, it was found that both the geometrical configuration and the electric potential distribution of the coordinated ligand played the critical roles in affecting the interfacial/interior electronic properties of perovskite photoactive layer. Relative to the non-conjugated and tortile aniline ligand with similar structure, conjugated aniline PPEA presents a quasi-coplanar configuration and distinct electron delocalization characteristic. Based on a moderate post-treatment process, PPEA molecules exhibited more favorable orientation on top of the perovskite film, contributing to the stronger dipole moment. Correspondingly, more suitable banding alignment can be achieved to boost the charge extraction and enlarge the built-in potential at the photoactive/transporting interface. Meanwhile, as for the modification of the 3D perovskite framework, “linear-style” $PPEA^+$ cation could form more ordered stacking/interactions across neighboring crystalline units/grains, providing more effective channels for charge transport. Relative to the reference device with the PCE of 17.47%, a champion PCE of 20.89% can be obtained from the device with optimal PPEA modification. This facial passivation route was also successfully applied to large-scale devices, presenting a 18.43% PCE with an area of 1.96 cm^2. Furthermore, with the moderate regulation of the post-treatment process, ultrathin 2D perovskite capping layer could in situ grow on the

3D framework, and this large-bandgap and hydrophobic passivation layer could further prevent the invasion of moisture and ion migration. Thus, the PPEA-modified PSC shows only 9.8% efficiency loss in dark condition (1000 h aging) and 10.4% in operating condition (200 h aging). To sum up, this "charge accelerating" conjugated ligand can substantially heal the traps and enhance device stability. We hope that our exploration could have the implications of the more effective interface engineering development, consequently breaking the performance bottleneck of the PSCs.

RESULTS AND DISCUSSION

Films and Materials Characteristics

To reveal the characteristic of the conjugated aniline ligand (3-phenyl-2-propen-1-amine [PPEA]) affecting the PSC performance, a non-conjugated molecule with similar structure, namely, 3-phenylpropylamine (PPA), was selected as a comparison (shown in Figure S1, Supporting Information). The interface passivation engineering was carried out via a post-treatment process, and the procedure of which was illustrated in Figure 1. For systematically studying the passivation mechanism, graded concentration of amine iodides solutions was designed. Correspondingly, the low-concentration (2 mm), medium-concentration (5 mm), and high-concentration (10 mm) post-treated perovskite films were named as L-PPEA(L-PPA), M-PPEA (M-PPA), and H-PPEA (H-PPA). First, the evolution of surface morphology of post-treatment perovskite films was investigated. Figure 1 and Figure S2 in the Supporting Information show the top-view SEM images of the pristine film and the corresponding modified films. We can observe that under a low treatment, there was unobvious morphology evolution on the surface of the perovskite films; as for the medium processing, tight integration of the polycrystal grains can be observed; with regard to the high-treated films, the distinct strip-like layer was formed instead of the original 3D morphology. The enormous morphological variation in medium-/high-treated films was speculated to the possibility of in situ grown capping layer, assisted by the large-sized organic cations with lower activation energy. To confirm our hypothesis, the absorption spectrum and X-ray diffraction (XRD) of a series of perovskite films were measured.

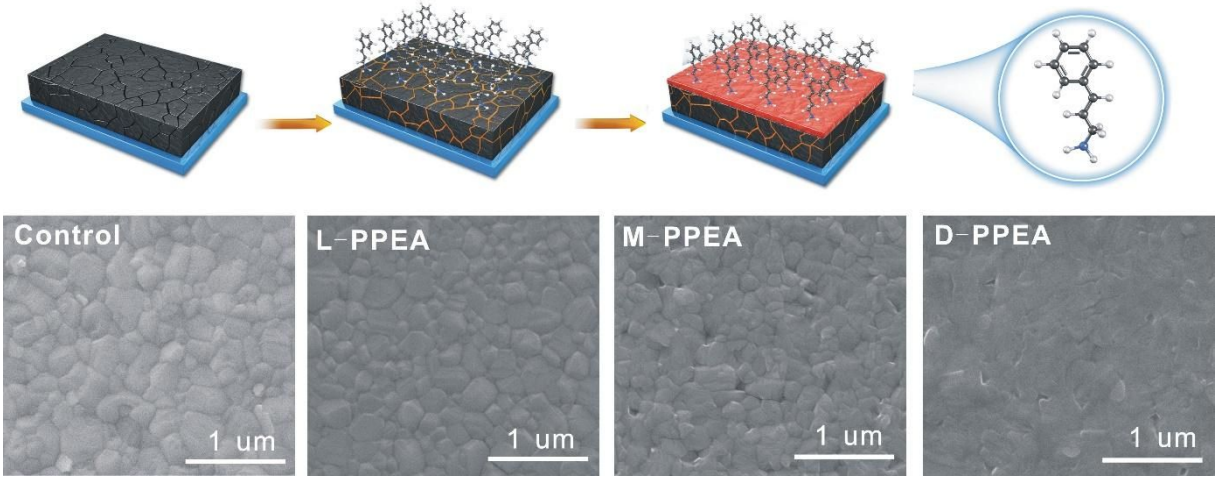

Figure 1. The procedure of the post-treatment process via anilines (up) and top-view SEM images of the pristine and PPEA-modified perovskite films (down).

The UV–vis absorption spectra of perovskite films are presented in Figure 2a and Figure S3a in the Supporting Information. As shown in the spectra, the pristine and modified films exhibit similar profile with an absorption band-edge with 780 nm, corresponding to the bandgap of $MAPbI_3$ [35]. Although a slightly improved absorbance of modified films was observed, which can be ascribed to the emerging perovskite capping layer, overall absorbance was almost invariant. Thus, the optical contribution of modified perovskite layer was negligible by post-treatment engineering.

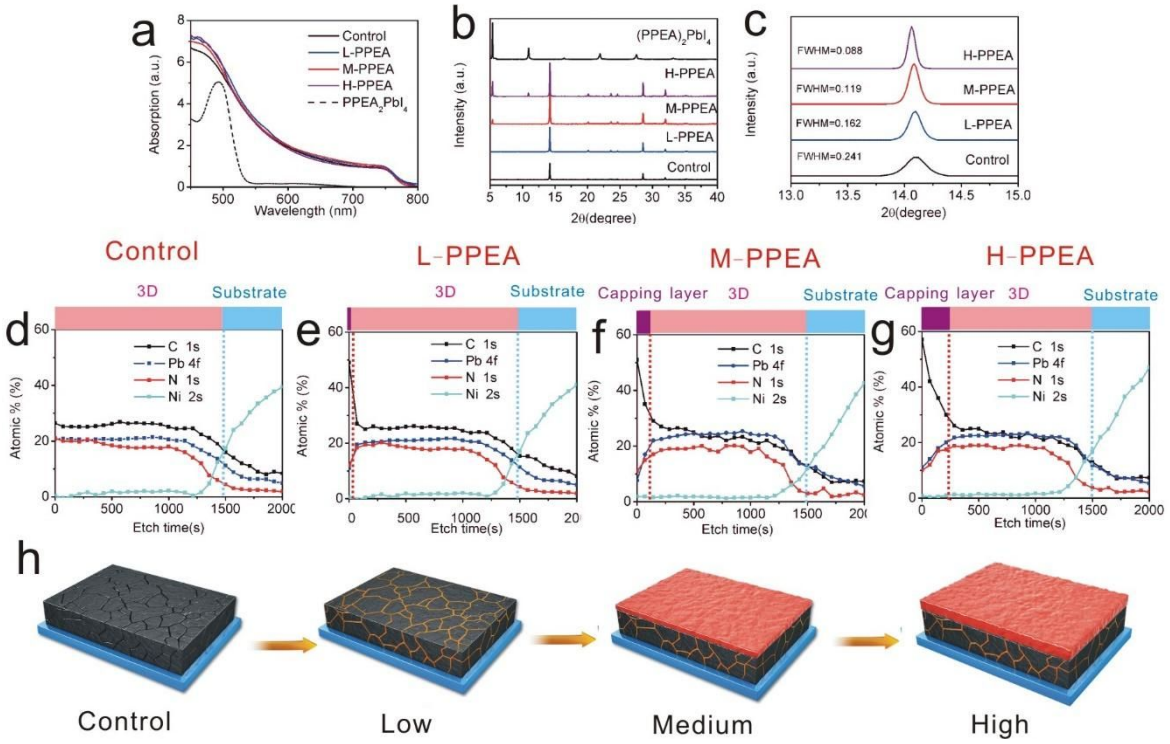

Figure 2. a) Optical absorption spectra of various perovskite films; b) XRD patterns of various perovskite films; c) magnified (110) peak of XRD patterns; d–g) depth XPS of controlled, L-PPEA, M-PPEA, and H-PPEA films; h) schematic diagram of the morphology and component variation with the controlled post-treatment.

The corresponding XRD patterns were measured and shown in Figure 2b and Figure S3b in the Supporting Information. The strong diffraction peaks at 14.1° and 28.2° can be assigned to the (110) and (220) characteristic crystal planes of $MAPbI_3$ [36]. Here the full width at half maximum (FWHM) and the position of the (110) peak pattern were further estimated in enlarged region (shown in Figure 2c). As treatment being intensive, gradually narrowed FWHM and increased intensity indicated the enhanced crystallization of $MAPbI_3$, which can be attributed to the progressive trap healing at the grain boundaries and the surface of the films. Notably, for M-PPEA (M-PPA) and H-PPEA (H-PPA) films, emerging featured peak appeared on the lower angle region. By comparing with the reference 2D perovskite films ($PPEA_2PbI_4$, PPA_2PbI_4), the peak positions we observed in the newly formed perovskite well agree with the typical 2D phase.

To further understand the structure and composition evolution of the perovskite films with the strengthening of the post-treatment tendency, depth profile analysis of X-ray photo-electron spectroscopy (D-XPS) was adopted [37]. In Figure 2d–g, the percentages of in-depth distribution of the atomic species on PPEA-modified films are shown as a function of the etching time. On account of the variation of the atomic percentages ratio, the composition variation along longitudinal direction of the perovskite bulk layer can be deduced indirectly. Figure 2d shows a homogeneous atomic percentage distribution of C, N, and Pb in the pristine perovskite film. As for the PPEA-modified films (Figure 2e–g), a rather high content of C atom decreased gradually through the near-surface of the film and then remained stable, whereas the content of Pb and N atoms had a contrast tendency compared with the C atom. Moreover, the higher the concentration treated, the wider the steep dropping region. Considering the different C atom ratio (37.5% and 80.6%) in two types of cations(MA^+ ($CH_3NH_3^+$) and $PPEA^+$ ($C_6H_5C_3H_4NH_3^+$)), the variation of the atomic percentage reflected the forming process of the graded 2D capping layer dependent on the concentrations of the treated PPEA solutions indirectly. Furthermore, cross-sectional SEM images of perovskite films were also measured and shown in Figure S4 in the Supporting Information. With the increase of the PPEA concentration, a thin in situ capping layer formed on the surface of the original film with smoother morphology, and the thicknesses of the 2D perovskite capping layers was in direct proportion to the concentration of PPEA solution.

Based on the analysis of XRD, D-XPS, and morphology variation, it is revealed that the concentration-controlled ligand treatment could achieve a gradual modification process on perovskite films: light treatment mainly affected the crystallinity of the 3D framework, maintaining the phase purity, whereas strong treatment could induce the emergence of the thickness-controlled capping layer, forming the 2D–3D bilayer structure. According to the above-measured properties dependent on ligand concentrations, irrespective of the class of ligand, we can deduce that perovskite phase is gradually transiting to 2D/3D hybrid as ligand increases. However, the ligand bonding interaction as well as the effect on intrinsic properties of perovskites still remains unclear.

J–V Characteristics

Above all, to comprehensively evaluate the characteristic of aniline ligands effect, planar inverted heterojunction structure devices with different photoactive films were fabricated. The device configuration designed in our study was fluorine doped tin oxide (FTO)/NiO_x/$MAPbI_3$/[6,6]-phenyl-C_{61}-butyric acid methyl ester (PCBM)/bathocuproine (BCP)/Ag, whose schematic architecture and the energy level diagram are illustrated in Figure 3a,b. To verify the reproducibility of our PSCs, the statistical photovoltaic parameters are summarized in Figure S5 and Table S1 in the Supporting Information (30 devices for each structure). The representative current density–voltage (*J–V*) curves of PSCs based on various modified films are shown in Figure 3c,d. Regardless of ligands, device performances were gradually increased from low to medium treatment but fell under high treatment, probably originating from crystal phase evolution: 1) Low treatment holding 3D structure could passivate partial ionic vacancies, where defects were not efficiently eliminated yet; 2) High treatment shall introduce undesirable 2D phase, curtailing charge transfer between interfaces upon perovskite; 3) Medium treatment seems to be the most reliable way for charge behavior and device robustness [25,38].

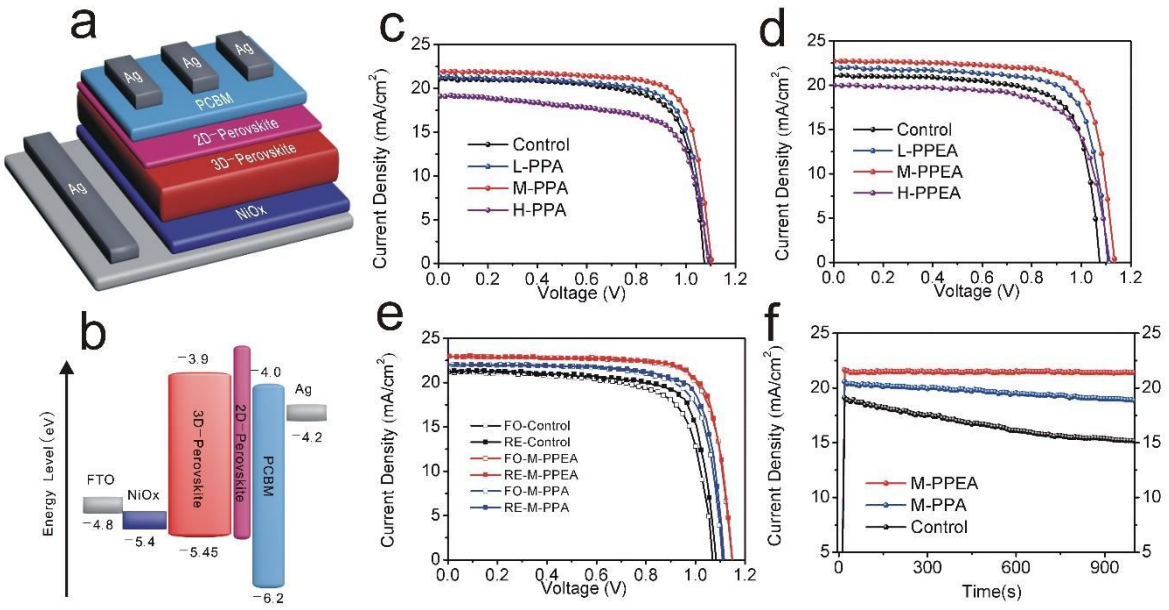

Figure 3. a,b) Device structure and energy diagram of the perovskite solar cells; *J–V* curves of PSCs with c) PPEA and d) PPA; e) J–V curves of the best PSCs; f) J–t curves of stabilized current density (V_{max} = 0.921 V for the best device with pristine film, V_{max} = 0.963 V for the best device with M-PPEA film, and V_{max} = 0.954 V for the best device with M-PPA film).

Then we focus on discrimination of device performance based on different ligands. Figure 3e shows the best performance PSCs under the reverse and forward scan, respectively, whose detailed parameters are presented in Table 1. The champion device with M-PPEA film exhibited the J_{sc} of 23.01 (22.98) mA cm^{-2}, V_{oc} of 1.148 (1.146) V, fill factor (FF) of 0.791 (0.781), and PCE of 20.89% (20.53%), while the champion device with M-PPA film exhibited the J_{sc} of 22.2 (21.99) mA cm^{-2}, V_{oc} of 1.119 (1.116) V, FF of 0.789 (0.761), and PCE of 19.51% (18.67%). Incident photons to current efficiency (IPCE) is shown in Figure S6 in the Supporting Information; it can be seen that the integration photocurrent density of the IPCE was consistent with the J_{sc} derived from the *J–V* curve. Considering the

performance reliability of controlled and modified PSCs, stabilized current density corresponding to maximum output power was measured and is shown in Figure 3f. The controlled device showed a distinct decay in current density during the testing process, while the devices with M-PPEA and M-PPA almost stabilized at the initial responding current density beginning to end, and the former device exhibited a little more stable output. The hysteresis and instability of J_{sc} was mainly due to the halide ion migration associated with phase segregation especially at grain boundaries. As for the device with aniline-modified films, photoinstability was alleviated by insertion of long-chain cations due to suppression of halide migration at grain boundaries. Particularly, the conjugated PPEA showed a more effective performance improvement compared with the non-conjugated PPA, embodying on both enhanced V_{oc} and J_{sc}. The discrepancy of device performance induced by passivation helped us to figure out the underlying causes.

Table 1. Photovoltaic parameters of champion devices based on different perovskite films measured in reverse and forward scan.

Sample	V_{oc} [V]	J_{sc} [mA cm^{-2}]	FF	PCE [%]
Control-Fo	1.072	21.22	0.724	16.47
Control-Re	1.081	21.32	0.768	17.70
M-PPEA-Fo	1.146	22.98	0.781	20.53
M-PPEA-Re	1.148	23.01	0.791	20.89
M-PPA-Fo	1.116	21.99	0.761	18.67
M-PPA-Re	1.119	22.03	0.789	19.51

Construction Tailoring and Interfacial Dipole

Theoretically, the open voltage of PSCs mainly depended on the splitting of electron and hole quasi-Fermi levels in the fabricated devices [27,39,40]. Previous studies have shown that as for the 2D–3D perovskite stacking-layered architecture, large-bandgap 2D perovskite capping layer could induce larger Fermi-level separation, in favor of the enhanced open-circuit voltage [41]. However, considering the similar bandgap of 2D-PPEA (E_g = 2.36 eV) and 2D-PPA (E_g = 2.38 eV) perovskite materials (Figure 2a; Figure S3c, Supporting Information), the Fermi-level splitting of aniline-modified devices should have little difference. Actually, unlike the small-sized and torsional MA^+ and FA^+ cations, long-chain and large-sized anilines have certain orientations due to the high steric hindrance and strong rigidity [32]. As for the representative post-treatment process, the aniline ligands could anchor to the surface of the perovskite film via incorporation of amino group with uncoordinated Pb–I bonds. Then a capping ligand layer formed at the interface of the perovskite/transporting layer, influencing on the interfacial polarization correspondingly. To investigate the energy level evolution of perovskite film, ultraviolet photoelectron spectroscopy (UPS) was adopted. Specifically, the work functions (W_F) and valence band (VB) level can be determined from the cutoff and Fermi edge of UPS spectra (shown in Figure S4, Supporting Information) on account of the expression W_F = 21.22 eV – E_{cutoff} and VB = 21.22 eV − (E_{cutoff} − E_{edge}) [27]. In this way, the W_F and VB for the pristine and anilines-modified perovskite film are estimated and shown in Figure 4b and Table S2 in the Supporting Information. For L-PPA and L-PPEA films, the shift of the VB level was negligible compared to that of the pristine film, illustrating that 2D capping layer was unformed. Interesting, the W_F of L-PPEA significantly downshifted 0.15 eV but the W_F of L-PPA only slightly downshifted 0.06 eV. Considering the comparable VB levels of the three films (pristine, L-PPA, and L-PPEA), we hypothesized that the WF modulation of anilines-modified films was concerned with the dipole effect induced by the coordinated interfacial molecular layer. As for the moderate and depth aniline-treatment films, the apparent shift of the VB level demonstrated the in situ growth of the 2D perovskite layers, and more positive WF shift of PPEA-modified films can be observed invariably.

Through the detailed comparison, stronger interfacial dipole moment can be induced by conjugated PPEA. To explore the origin of the interfacial dipole, geometric optimizations of PPEA and PPA were calculated by density functional theory implemented in the Gaussian 09 package (in vacuum environment), the results of which are shown in Figure 5. At the lowest energy conformation, PPEA showed a quasi-coplanar structure, while PPA exhibited a relative distorted

configuration. As for the dihedral angle of molecules between benzene part and allyl/alkyl part, the values of PPEA and PPA are ≈1.62° and ≈84.61°, respectively. Hence, we surmised that PPEA exhibiting the smaller tilted angle could present preferable molecular orientation on the surface of the perovskite film. Moreover, electrostatic surface potential (ESP; electronegative part is green and electropositive part is blue) of two types of aniline molecules was also carried out and is shown in Figure 5. It can be seen that obvious electronic delocalization occurred in PPEA, whereas PPA emerged in an entangled state. Considering that PPEA and PPA consisted of same head/trail groups and similar chain, C–C bond of the branched chain effectively strengthened the conjugated characteristics of the molecules, determining the planarity and delocalization in PPEA. From calculation, PPEA induced a larger component of dipole moment normal to the surface (2.82 D) than PPA (1.15 D) (details shown in the Supporting Information). Benefiting from the distinctive geometry and ESP of conjugated PPEA aniline, much stronger interfacial dipole was formed at the perovskite/electron transport layer (ETL). Such a stronger interfacial dipole moment could further achieve the band alignment and reinforce the built-in electric force across the interface, thereby facilitating the charge extraction and providing higher improvements in V_{oc}.

As further evidence, we also carried out the Mott–Schottky measurement to analyze the variation of the built-in potential of different devices (shown in Figure 4c). The built-in potential was derived from the capacitance–voltage measurement, according to the following equation [42]:

$$\frac{1}{C^2} = \frac{2}{\varepsilon\varepsilon_0 q A^2 N}(V_{fb} - V) \quad (1)$$

where C represents the measured capacitance, A is the active area, V the applied bias, ε is the static permittivity, ε_0 is the vacuum permittivity, q is the elementary charge, and N is the doping density, and V_{fb} is the built-in potential (V_{bi}). It was found that the V_{bi} of devices with pristine film, M-PPA film, and M-PPEA film were 1.061, 1.098, 1.131 V, respectively, which agree well with the interfacial dipole characteristic and device performance.

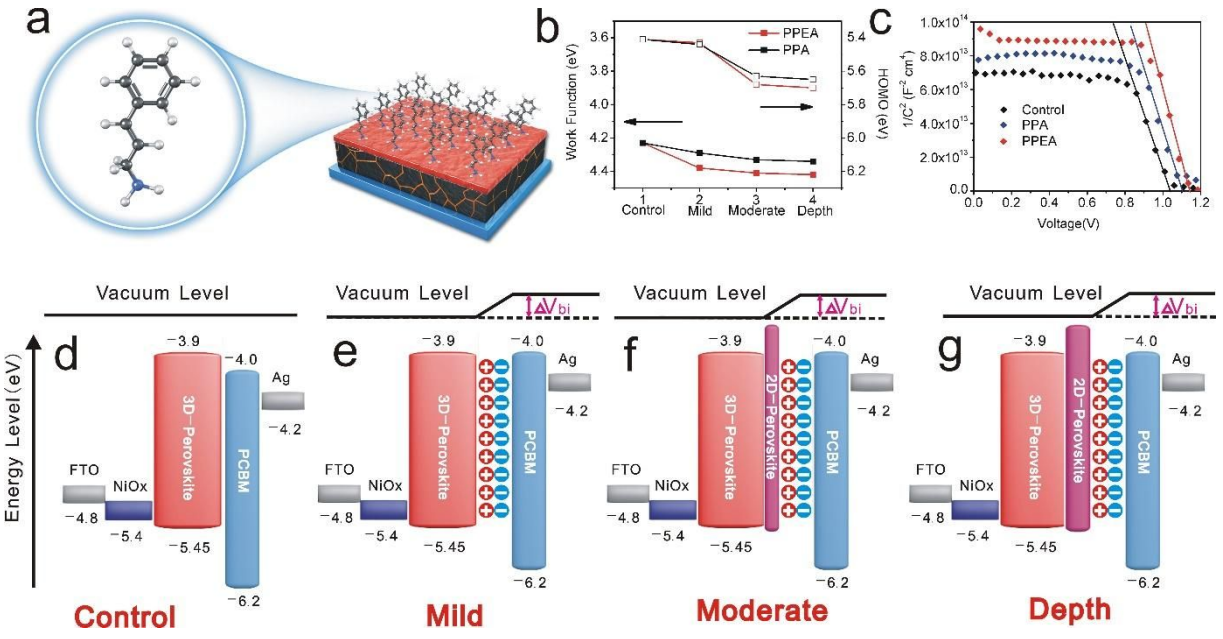

Figure 4. a) Schematic diagram of in situ growth capping layer and interfacial dipole layer; b) W_F and VB variation of different perovskite films; c) Mott–Schottky curves of the various devices with pristine and best-modified films (control, M-PPA, and M-PPEA); d–f) schematic diagram of the interfacial dipole moments and emerged 2D capping layer accompanying with the controlled treatment process.

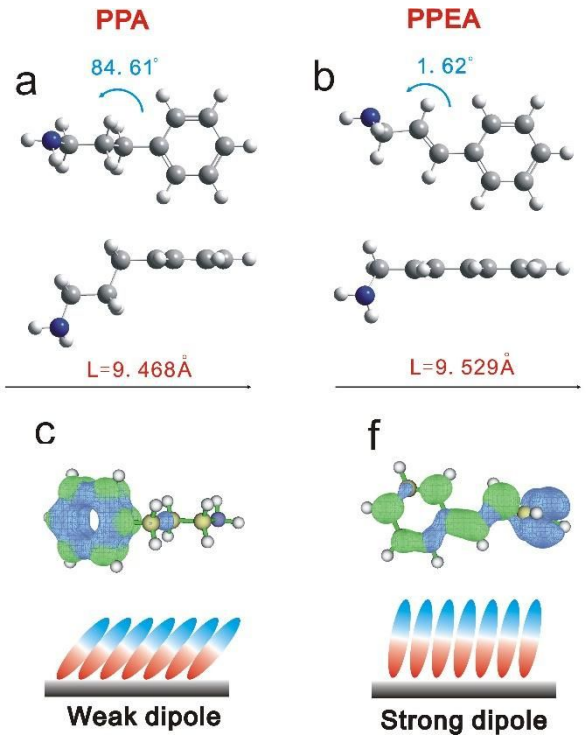

Figure 5. Geometric optimizations of a,b) PPA and c,d) PPEA; ESP of e) PPA and f) PPEA; calculated by density functional theory implemented in the Gaussian 09 package (electronegative part is green and electropositive part is blue).

Establishment of the Interior Charge Transporting Network

In addition to the remarkable improvement of the open voltage, conjugated PPEA-modified device also exhibited the superior photocurrent performance. Actually, conventionally modified ligands struggled with the long-chain/large-size structure and weak-delocalization electrical properties, supplying a limited contribution to the improvement of the photocurrent [7,38]. It was known that photocurrent density was closely related to both the interface and the interior electrical properties of the photoactive bulk film [14]. Therefore, verification of the interior electron dynamics process of the photoactive film, especially in the dominated 3D framework, was essential to further understand the advantages of the conjugated modifier. To intuitively investigate the inherent electrical property of the perovskite films, especially in the dominated 3D framework, an etch process (1000 s) was procured for three perovskite films (pristine, M-PPA, and M-PPEA) first, ensuring removing the 2D capping layer and partial upper 3D layer. XPS measurement was carried out to elucidate the coordination of the long-chain ligands. Figure S8 in the Supporting Information presents XPS spectra of the Pb 4f peaks in controlled, M-PPA, and M-PPEA films. Compared with the controlled film, the peaks of Pb 4f7/2 and Pb 4f5/2 in M-PPA and M-PPEA films shifted to lower binding energy. The shift of Pb 4f toward low binding energy reflected the longer Pb–I bond, which can be attributed to the coordination of long-chain ligands with the perovskite bulk. Here the current atomic force microscopy (c-AFM) measurement was also carried out. Figure S9 in the Supporting Information shows the c-AFM images of the perovskite films after etch. Compared with controlled film, higher conducting current distribution of aniline-modified films was observed ($Peak_{control}$ = 93 nA, $Peak_{PPA}$ = 101 nA, $Peak_{PPEA}$ = 119 nA), indicating the improved charge transport characteristic in the absorber bulk. Moreover, in Figure S9g–i in the Supporting Information, obvious “trailer” can be observed in controlled film, which reflected the current leakage at the grain boundaries. As comparison, the undesirable “trailer” was gradually healed in ligands modified films. M-PPEA film exhibited the highest and most homogeneous current distribution, illustrating the significant passivation ability for the interior of the photoactive film.

Transient photocurrent measurements(TPC) were also employed to investigate the carrier dynamics across the entire framework in the completed devices. Figure 6a shows the TPC of the devices with different perovskite films (control, M-PPA, and M-PPEA). The M-PPA-based device just exhibited a slightly decreased photocurrent decay (1.18 μs) than the controlled device(1.29 μs). However, the photocurrent decay time of the device with M-PPEA significantly

reduced to 0.91 μs. Typically, a faster photocurrent decay time was accompanied with a more efficient charge transfer in the device [14]. Both the c-AFM and TPC measurements revealed the influence of the coordinated ligands on charge transporting/exchange in perovskite bulk.

In the as-prepared perovskite bulk, inevitable dangling bonds at the bare boundaries of adjacent grains/units would introduce the trap states and nonradiative recombination centers, adverse to the charge exchange across the entire perovskite framework [13,43,44], while the introduction of the coordinated ligands could effect on the interior of the perovskite bulk. The DFT simulation [45,46] of the steric arrangement of the aniline molecules on the surface of perovskite grains/units is shown in Figure 6c (details shown in the Supporting Information). It was found that tortile PPA oriented in the small angle (29°) on the surface of perovskite units, and the capping ligands just stayed away from each other between adjacent perovskite units, against the charge exchange. By contrast, PPEA molecules were packed almost perpendicular to the perovskite surface (69°), and the capping ligands could embed in each other between adjacent perovskite units. Here the effective overlap of coordinated cations in PPEA-modified film would promote the charge exchange/transport between neighboring units, thus contributing to the charge transporting in the perovskite bulk.

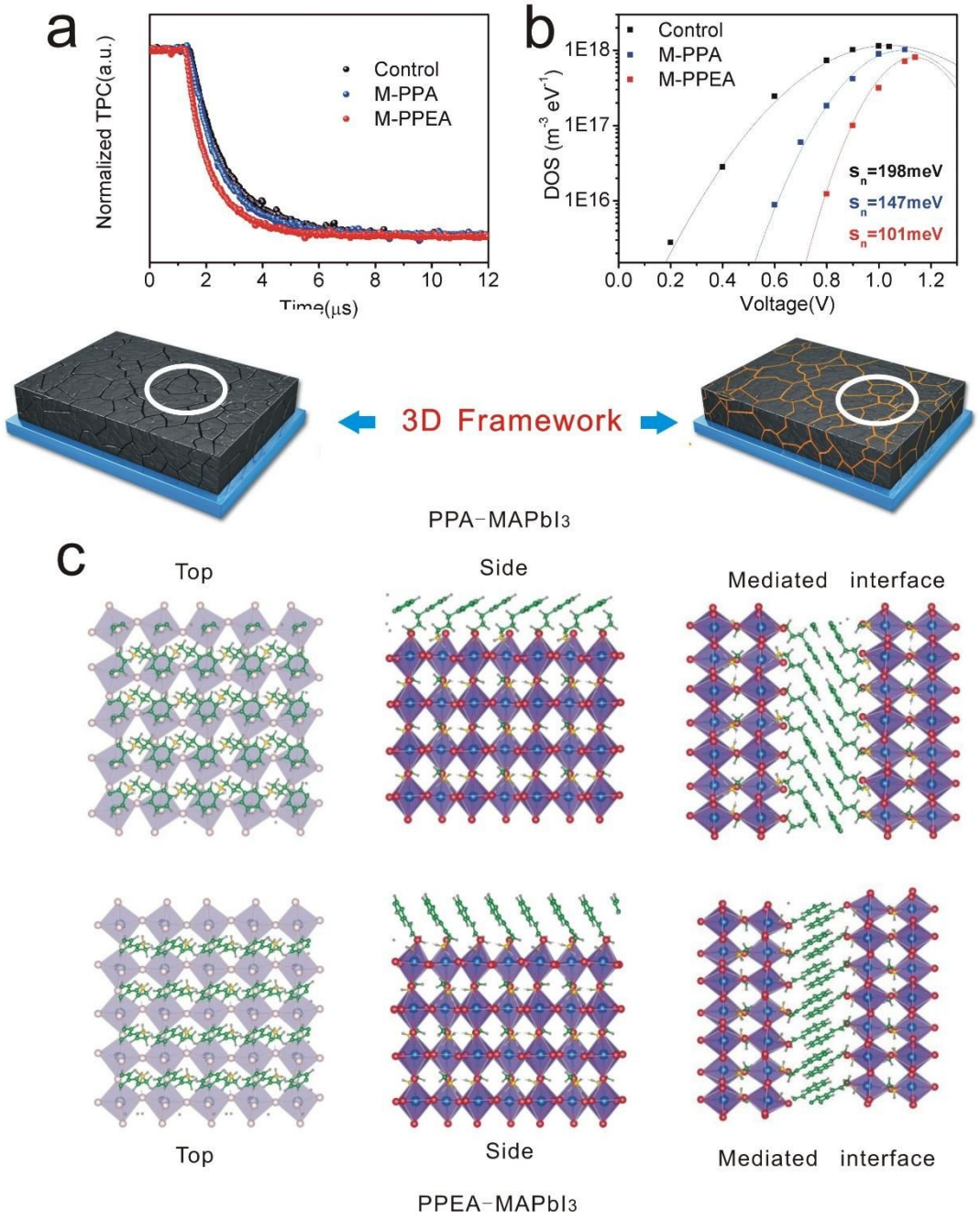

Figure 6. a) Transient photocurrent of PSCs with pristine film, M-PPEA film, and M-PPA film; b) electron density of states analysis of PSCs with pristine film, M-PPEA film, and M-PPA film; c) DFT simulation of the steric arrangement of the amine molecules on the surface of perovskite grains/units (C, N, H, Pb, and I atoms are colored in green, yellow, gray, blue, and red, respectively).

The energy disorder of the whole device was characterized to verify the theoretical analysis. The energy disorder is an explicit expression of the density of states (DOS) under a non-equilibrium state that can be induced by external driving force [40,47]. The DOS of electrons in the device can be achieved by the chemical capacitance (Cμ) by means of impedance spectroscopy. By adjusting the illumination driving force, the DOS can be estimated from the C_μ dependence on V_{oc}.

$$C_{\mu}^{(n)} = Lq^2 \frac{dn}{dE_{Fn}} \quad (2)$$

where n is the charge carrier density, L is the thickness of photoactive layer, and q is the elementary charge. We employed the Gaussian approximation to fit the DOS according to the following expression:

$$g_n(E - E_L) = \frac{N_n}{\sqrt{2\pi}} exp[-\frac{(E-E_L)^2}{2\sigma_n^2}] \quad (3)$$

where N_n is the total density, E_L is the energy center of the DOS, and σ_n is the disorder parameter corresponding to the

broadening of the DOS. As shown in Figure 6b, the device with controlled film, M-PPA film, and M-PPEA film showed the σ_n of 101, 147, and 198 meV, respectively. The narrowest DOS of the device with M-PPEA presented the least energy disorder states, which suggested the most preferable structure order. Based on the theoretical and experimental analysis, we proposed that the passivated PPEA ligands could effectively crosslink the perovskite crystalline grains/units and enhance the electronic coupling behavior, which played the role of electrical channel across the neighboring perovskite grains/units.

As just other evidence of the structure orientation variation effected by aniline passivation, grazing-incidence wide-angle X-ray scattering (GIWAXS) was utilized to investigate the crystal features in the pristine and aniline-treated perovskite films [48]. Figure S10a–c in the Supporting Information shows the 2D GIWAXS patterns of pristine and aniline-modified perovskite films (control, M-PPA, and M-PPEA). The peak in the out-of-plane direction at q = 10 nm^{-1} corresponded to the (110) diffraction peak of MAPbI3 perovskite. Results showed the stronger intensity of the (110) peak of M-PPA and M-PPEA compared with that of pristine film, indicating improved crystallization for aniline-modified perovskite films. As for the variation of the crystal orientation, scattering intensity of GIWAXS patterns along the ring at q = 10 nm^{-1} was azimuthally integrated. Compared to the pristine film, shaper peaks distributed at the azimuth angles between 0° and 180° were observed for M-PPEA and M-PPA films. These results indicated that relatively ordered orientations of perovskite framework were formed by aniline treatment, where conjugated PPEA cation could encourage
more preferable orientation of the bulk.

With a view to the delocalization characteristic of the conjugated aniline, the dissociation of photon-generated excitons in aniline-modified devices should be considered. To indirectly exploring the effect of aniline fragments in modified devices, the exciton binding energy (E_{eb}) of 2D $PPEA_2PbI_4$ and PPA_2PbI_4 was calculated (shown in Figure S11, Supporting Information). By fitting the integrated photoluminescence, we determined the E_{eb} of 197 and 226 meV for 2D $PPEA_2PbI_4$ and PPA_2PbI_4, respectively. Researches have reported that 2D perovskite has much larger exciton binding energy compared with the conventional 3D perovskite; thus, the introduction of the long-chain cation turned against the dissociation of photon-generated excitons to some extent [49]. However, differing from more traditional PPA, the relatively low E_{eb} of the PPEA will have little effect on exciton dissociations, significantly improving free carrier populations.

Large-Scale Application and Stability

Both the high quality of the perovskite film and efficient interface charge transfer in our inverted device offered a potential platform for large-area cells. Here we fabricated the device with a 1.5×1.5 cm^2 active areas (with a 1.4×1.4 cm^2 mask) by employing the M-PPEA film, and correspondingly a considerable performance of 18.43% was achieved with J_{sc}, V_{oc}, and FF reaching 21.98 mA cm^{-2}, 1.105 V, and 0.755, respectively (shown in Figure 7a). Compared with the small-sized device, the slight decrease of PCE in large-size cells was mainly caused by the relatively low conductivity of FTO substrate. Here, the reproducibility with narrow distribution for these large-area devices was also verified. We measured *J–V* curves at four different small spots (each 0.3 cm × 0.3 cm) located at the corners of the active area. All the PV metrics are almost identical, confirming the expansibility of this typical conjugated-ligands passivation engineering on the square-centimeter scale.

In addition to the high photovoltaic efficiency of the PSCs, another major concern was the durability for long-term applications. We therefore checked the stability of the perovskite films as well as the corresponding devices. Accordingly, the degradation process can be traced through the change in the film color and the evolution of XRD measurements (shown in Figure S12, Supporting Information). As seen from XRD, no decomposition of the perovskite was observed in M-PPEA film after 90 days in air condition, indicating that the passivated sample was robust enough to sustain moisture and oxygen, whereas the precipitation of the PbI_2 of controlled film emerged with time. As shown in Figure S8 in the Supporting Information, a rather large contact angle (θ = 85°) of the M-PPEA was observed compared to that of the pristine film (θ = 39°). As for the devices, all the samples were stored under dark or light illumination without encapsulation in a dry cabinet at 25°C and with ≈40% relative humidity. Impressively, the device with M-PPEA retained 90.2%/89.6% of its initial performance after 1000 h/200 h of dark/illumination condition (Figure 7b,c). On the contrary, the device based on pristine 3D perovskite showed the faster degradation of

performance. Actually, in situ grown 2D capping layer in PPEA-modified film could serve as a self-encapsulating "cover," deterring the moisture attack. Meanwhile, the long-chain cations anchored on the surface of the perovskite GBs and units could further prevent the ion migration when device operating.

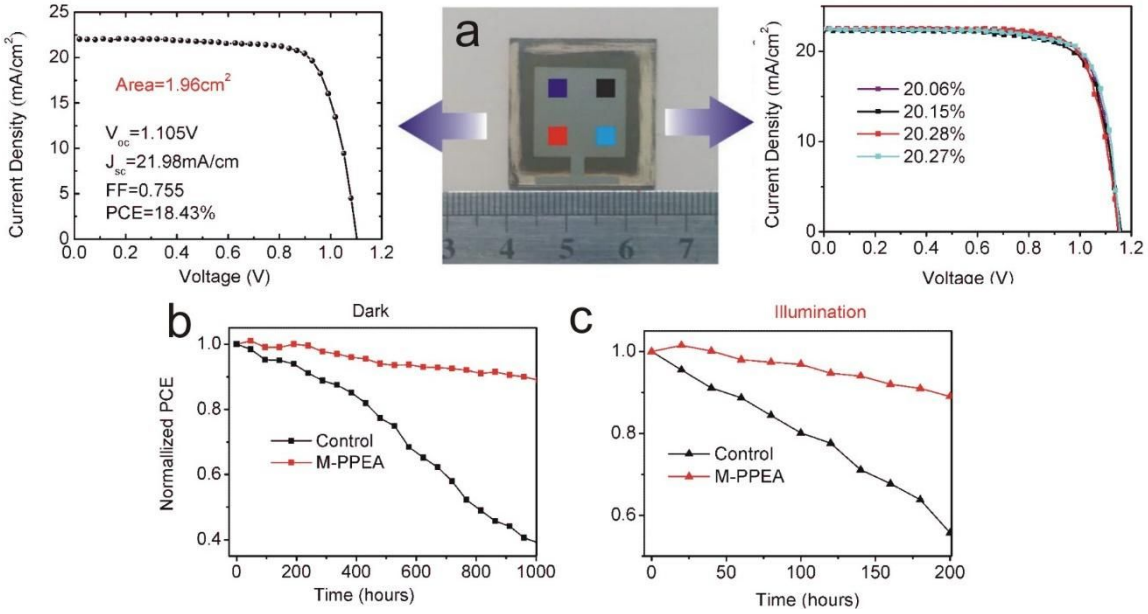

Figure 7. a) *J–V* curves measurements of large area (1.96 cm^2) and small region devices (0.09 cm^2); b) dark stability and c) working stability (1 sun illumination) of the devices with pristine and M-PPEA films.

CONCLUSIONS

In summary, an innovative conjugated aniline PPEA was developed to simultaneously improve the performance and stability of the PSCs. Our study emphasized that both the geometrical configuration and the electric potential distribution of the molecules are of critical importance for the crystallinity and interfacial/interior charge dynamic process of perovskite photoactive layer. Under particular treatment of such conjugated quasi-planar ligands, matched band alignment, enlarged built-in potential, and enhanced charge extraction are achieved on account of substantially strengthened dipole moment. Furthermore, suppression of surface defects and acceleration of charge transport are available involved with overlapping of modified grain/units. Thanks to aforementioned advantages of this novel ligands assembled upon perovskite, nearly 21% efficiency of the best solar cell can be realized, accompanying with a long-term stability (maintaining 90.2% of initial PCE after 1000 h testing, 25°C, and 40 ± 10 humidity). This effective and facile approach can also make the large-scale success, with a performance of 18.43% at the area of 1.96 cm2. We expect that our work could inspire the prospects of passivators design, sequentially further promoting performance and stability of the PSCs.

ACKNOWLEDGEMENTS

This work was financially supported by National Natural Science Foundation of China (Grant Nos. 11574248, 61604121, 61505161), National Key R&D Program of China (Grant No. 2016YFB0400702), China Postdoctoral Science Foundation (Grant No. 2016M590947), Scientific Research Plan Projects of Shaanxi Education Department (Grant No. 17JK0700), Natural Science Basic Research Plan in Shaanxi Province of China (Grant No. 2016JM6024, 2017JM6064), Fundamental Research Funds for the Central Universities (Grant No. xjj2016031), and the Global Frontier R&D Program of the Center for Multiscale Energy System (Grant No. 2012M3A6A7054855). The SEM work was performed at International Center by Dielectric Research (ICDR), Xi'an Jiaotong University, Xi'an, China. The authors thank Dai and Ma for their help in using SEM. We also thank Dr. Liu at Instrument Analysis Center of Xi'an Jiaotong University for her assistance with UPS and XPS analysis. J.L. thanks the generous allocation of computing resources by the CSC – IT Center for Science (Project No. ay6311), the Aalto Science-IT project, and the

Innovative and Novel Computational Impact and Theory and Experiment (INCITE) program by the Argonne Leadership Computing Facility (Contract No. DE-AC02-06CH11357).

References

1. W. Y. Nie, H. H. Tsai, R. Asadpour, J. C. Blancon, A. J. Neukirch, G. Gupta, J. J. Crochet, M. Chhowalla, S. Tretiak, M. A. Alam, H. L. Wang, A. D. Mohite, Science 2015, 347, 522.
2. S. D. Stranks, G. E. Eperon, G. Grancini, C. Menelaou, M. J. P. Alcocer, T. Leijtens, L. M. Herz, A. Petrozza, H. J. Snaith, Science 2013, 342, 341.
3. Y. F. Shi, W. Wu, H. Dong, G. R. Li, K. Xi, G. Divitini, C. X. Ran, F. Yuan, M. Zhang, B. Jiao, X. Hou, Z. X. Wu, Adv Mater 2018, 30.
4. A. Kojima, K. Teshima, Y. Shirai, T. Miyasaka, J Am Chem Soc 2009, 131, 6050.
5. https://www.nrel.gov/pv/assets/images/effciency-chart.png.
6. H. S. Kim, C. R. Lee, J. H. Im, K. B. Lee, T. Moehl, A. Marchioro, S. J. Moon, R. Humphry-Baker, J. H. Yum, J. E. Moser, M. Gratzel, N. G. Park, Sci. Rep. 2012, 2, 591.
7. K. T. Cho, G. Grancini, Y. Lee, E. Oveisi, J. Ryu, O. Almora, M. Tschumi, P. A. Schouwink, G. Seo, S. Heo, J. Park, J. Jang, S. Paek, G. Garcia-Belmonte, M. K. Nazeeruddin, Energ Environ Sci 2018, 11, 952.
8. J. Z. Chen, J. Y. Seo, N. G. Park, Adv Energy Mater 2018, 8.
9. F. Yuan, J. Xi, H. Dong, K. Xi, W. W. Zhang, C. X. Ran, B. Jiao, X. Hou, A. K. Y. Jen, Z. X. Wu, Phys Status Solidi-R 2018, 12.
10. W. J. Yin, T. T. Shi, Y. F. Yan, Appl Phys Lett 2014, 104.
11. X. P. Zheng, B. Chen, J. Dai, Y. J. Fang, Y. Bai, Y. Z. Lin, H. T. Wei, X. C. Zeng, J. S. Huang, Nat Energy 2017, 2.
12. M. J. Yang, Y. N. Zeng, Z. Li, D. H. Kim, C. S. Jiang, J. van de Lagemaat, K. Zhu, Phys Chem Chem Phys 2017, 19, 5043.
13. T. Zhao, C. C. Chueh, Q. Chen, A. Rajagopal, A. K. Y. Jen, Acs Energy Lett 2016, 1, 757.
14. Z. G. Xiao, Q. F. Dong, C. Bi, Y. C. Shao, Y. B. Yuan, J. S. Huang, Adv Mater 2014, 26, 6503.
15. Y. H. Shao, Z. G. Xiao, C. Bi, Y. B. Yuan, J. S. Huang, Nat Commun 2014, 5.
16. Y. Bai, X. Y. Meng, S. H. Yang, Adv Energy Mater 2018, 8.
17. A. B. Yusoff, P. Gao, M. K. Nazeeruddin, Coordin Chem Rev 2018, 373, 258.
18. H. J. Snaith, Nat Mater 2018, 17, 372.
19. T. Lei, H. Dong, J. Xi, Y. Niu, J. Xu, F. Yuan, B. Jiao, W. W. Zhang, X. Hou, Z. X. Wu, Chem Commun 2018, 54, 6177.
20. P. Schulz, Acs Energy Lett 2018, 3, 1287.
21. A. Fakharuddin, L. Schmidt-Mende, G. Garcia-Belmonte, R. Jose, I. Mora-Sero, Adv Energy Mater 2017, 7.
22. J. Huang, Y. Yuan, Y. Shao, Y. Yan, Nat Rev Mater 2017, 2.
23. Y. Hu, Z. H. Zhang, A. Y. Mei, Y. Y. Jiang, X. M. Hou, Q. F. Wang, K. Du, Y. G. Rong, Y. H. Zhou, G. Z. Xu, H. W. Han, Adv. Mater. 2018, 30, 1705786.
24. F. Wang, W. Geng, Y. Zhou, H. H. Fang, C. J. Tong, M. A. Loi, L. M. Liu, N. Zhao, Adv Mater 2016, 28, 9986.
25. Y. Bai, S. Xiao, C. Hu, T. Zhang, X. Y. Meng, H. Lin, Y. L. Yang, S. H. Yang, Adv Energy Mater 2017, 7, 1701038.
26. K. M. M. Salim, T. M. Koh, D. Bahulayan, P. C. Harikesh, N. F. Jamaludin, B. Febriansyah, A. Bruno, S. Mhaisalkar, N. Mathews, Acs Energy Lett 2018, 3, 1068.
27. J. F. Lu, X. F. Lin, X. C. Jiao, T. Gengenbach, A. D. Scully, L. C. Jiang, B. Tan, J. S. Sun, B. Li, N. Pai, U. Bach, A. N. Simonov, Y. B. Cheng, Energ Environ Sci 2018, 11, 1880.
28. C. X. Ran, J. Xi, W. Y. Gao, F. Yuan, T. Lei, B. Jiao, X. Hou, Z. X. Wu, Acs Energy Lett 2018, 3, 713.
29. H. Zhang, X. G. Ren, X. W. Chen, J. Mao, J. Q. Cheng, Y. Zhao, Y. H. Liu, J. Milic, W. J. Yin, M. Gratzel, W. C. H. Choy, Energ Environ Sci 2018, 11, 2253.
30. T. Ye, A. Bruno, G. F. Han, T. M. Koh, J. Li, N. F. Jamaludin, C. Soci, S. G. Mhaisalkar, W. L. Leong, Adv Funct Mater 2018, 28.
31. T. Q. Niu, J. Lu, R. Munir, J. B. Li, D. Barrit, X. Zhang, H. L. Hu, Z. Yang, A. Amassian, K. Zhao, S. Z. Liu, Adv Mater 2018, 30.
32. W. H. Lee, C. Y. Chen, C. S. Li, S. Y. Hsiao, W. L. Tsai, M. J. Huang, C. H. Cheng, C. I. Wu, H. W. Lin, Nano Energy 2017, 38, 66.
33. Y. Z. Lin, L. Shen, J. Dai, Y. H. Deng, Y. Wu, Y. Bai, X. P. Zheng, J. Y. Wang, Y. J. Fang, H. T. Wei, W. Ma, X. C. Zeng, X. W. Zhan, J. S. Huang, Adv Mater 2017, 29.

34. B. B. Cui, N. Yang, C. B. Shi, S. S. Yang, J. Y. Shao, Y. Han, L. Z. Zhang, Q. S. Zhang, Y. W. Zhong, Q. Chen, J Mater Chem A 2018, 6, 10057.
35. H. Dong, Z. X. Wu, J. Xi, X. B. Xu, L. J. Zuo, T. Lei, X. G. Zhao, L. J. Zhang, X. Hou, A. K. Y. Jen, Adv Funct Mater 2018, 28.
36. H. S. Kim, J. Y. Seo, N. G. Park, Chemsuschem 2016, 9, 2528.
37. F. Matteocci, Y. Busby, J. J. Pireaux, G. Divitini, S. Cacovich, C. Ducati, A. Di Carlo, Acs Appl Mater Inter 2015, 7, 26176.
38. P. Chen, Y. Bai, S. C. Wang, M. Q. Lyu, J. H. Yun, L. Z. Wang, Adv Funct Mater 2018, 28.
39. J. H. Lee, J. Kim, G. Kim, D. Shin, S. Y. Jeong, J. Lee, S. Hong, J. W. Choi, C. L. Lee, H. Kim, Y. Yi, K. Lee, Energ Environ Sci 2018, 11, 1742.
40. X. W. Hu, X. F. Jiang, X. B. Xing, L. Nian, X. Y. Liu, R. Huang, K. Wang, H. L. Yip, G. F. Zhou, Sol Rrl 2018, 2.
41. D. Y. Luo, W. Q. Yang, Z. P. Wang, A. Sadhanala, Q. Hu, R. Su, R. Shivanna, G. F. Trindade, J. F. Watts, Z. J. Xu, T. H. Liu, K. Chen, F. J. Ye, P. Wu, L. C. Zhao, J. Wu, Y. G. Tu, Y. F. Zhang, X. Y. Yang, W. Zhang, R. H. Friend, Q. H. Gong, H. J. Snaith, R. Zhu, Science 2018, 360, 1442.
42. H. Dong, T. Lei, F. Yuan, J. Xu, Y. Niu, B. Jiao, Z. X. Zhang, D. W. Ding, X. Hou, Z. X. Wu, Org Electron 2018, 60, 1.
43. N. Li, Z. L. Zhu, C. C. Chueh, H. B. Liu, B. Peng, A. Petrone, X. S. Li, L. D. Wang, A. K. Y. Jen, Adv Energy Mater 2017, 7.
44. J. F. Dai, J. Xi, L. Li, J. F. Zhao, Y. F. Shi, W. W. Zhang, C. X. Ran, B. Jiao, X. Hou, X. H. Duan, Z. X. Wu, Angew Chem Int Edit 2018, 57, 5754.
45. J. R. Li, M. Bouchard, P. Reiss, D. Aldakov, S. Pouget, R. Demadrille, C. Aumaitre, B. Frick, D. Djurado, M. Rossi, P. Rinke, J Phys Chem Lett 2018, 9, 3969.
46. J. R. Li, P. Rinke, Phys. Rev. B 2016, 94, 045201.
47. Y. C. Shao, Y. B. Yuan, J. S. Huang, Nat Energy 2016, 1.
48. F. C. Li, J. Y. Yuan, X. F. Ling, Y. N. Zhang, Y. G. Yang, S. H. Cheung, C. H. Y. Ho, S. K. So, X. Y. Gao, W. L. Ma, Adv Funct Mater 2018, 28.
49. J. Li, L. H. Luo, H. W. Huang, C. Ma, Z. Z. Ye, J. Zeng, H. P. He, J Phys Chem Lett 2017, 8, 1161.